Journal of Computational Physics **171,** 47–78 (2001)
doi:10.1006/jcph.2001.6763, available online at http://www.idealibrary.com on IDEAL®

Particle-in-Cell Simulation of Electrical Gas Discharges[1]

C. Soria,* F. Pontiga,† and A. Castellanos*

*Dpto. Electrónica y Electromagnetismo, Facultad de Física, Universidad de Sevilla, Av. Reina Mercedes s/n, 41012 Seville, Spain; and †Dpto. Física Aplicada, E. U. Arquitectura Técnica, Universidad de Sevilla, Av. Reina Mercedes s/n, 41012 Seville, Spain

E-mail: cshoyo@cica.es, pontiga@cica.es, castella@cica.es

Received May 2, 2000; revised February 1, 2001

A fluid particle-in-cell (PIC) model is proposed for the numerical solution of the continuity equation of electrons and ions in transient electrical gas discharges. The reactions occurring in a gaseous discharge, such as ionization of neutral molecules, electron attachment, and recombination between electrons and ions, are implemented through the variation of the mass of the computational particles used in the simulation. Two different forms of interpolation of the gain/loss rates from the grid to the computational particles are suggested, depending on the reaction type. The PIC model is first applied to the problem of an idealized electron avalanche in a non-attaching gas. This problem possesses an analytical solution where the electron density grows exponentially in time as it propagates, but keeps the square-wave form of the initial electron distribution. This problem is used to validate the optimum interpolation of the gain/loss rate and to analyze the effect of the mass matrix formulation of the PIC model. Then, a more realistic model is applied to simulate the propagation of a Trichel pulse between a sphere and a plate. In this case, the continuity equation for electrons and positive and negative ions, coupled to the Poisson equation, has been solved. This second test has proved the ability of the present numerical method to deal with those discharges dominated by the space charge effect. The results of the PIC simulation are compared with those obtained from the application of a flux-corrected transport method.

Key Words: 77xx; 77F05; 77H05; particle-in-cell; gas discharges; source terms; gain/loss rate; continuity equation; space charge.

1. INTRODUCTION

Electrical gas discharges are the result of many complex reactions that occur both in the bulk of a gas and at electrodes. In the bulk, electrons are accelerated by the electric

[1] This work has been supported by the Spanish DGICYT, under Contract PB96-1375.

0021-9991/01 $35.00

field and can ionize the surrounding region, thus producing positive ions. Also, electrons can attach to neutral molecules to form negative ions, and electrons and negative ions can recombine with positive ions to form again neutral molecules. At the electrodes, secondary electrons can be released by the impact of ions and/or photons generated in the bulk. All these reactions develop in very short times, typically a few hundreds of nanoseconds.

Many different numerical methods have been commonly applied to simulate the propagation and time evolution of gaseous discharges, such as hybrid methods of characteristics [1, 9, 25], flux-corrected transport (FCT) methods [11, 15, 20, 21], finite element (FE) methods [26], and, more recently, mixed FE–FCT methods [12, 13]. Even though particle-in-cell (PIC) methods are certainly leading methods in the area of plasma kinetic simulations [5, 14], PIC fluid models have not been so commonly applied to the simulation of gaseous discharges. However, some relevant works have recently appeared, particularly in the area of stationary glow discharges [17].

PIC methods have the advantage of being numerically less diffusive than most of the others numerical techniques. This fact guarantees the high accuracy of the simulation, both in transient and in stationary problems [7, 8, 17]. Moreover, its extension to 2D and 3D poses no additional problems. The major drawback of PIC methods is that they usually require longer computational times than other methods, like FCT for example. Nevertheless, this inconvenience is progressively losing strength as the power of computers increases steadily. For example, the simulations described in this paper were all carried out using a personal computer.

In this paper, a PIC method is formulated and applied to the numerical solution of the continuity equation of charge carriers created by an electrical gas discharge. In particular, this study is concerned with transient gas discharges where the space charge effects can lead to strongly non-uniform electric fields and very steep density gradients, as occurs in the development of Trichel pulses, the propagation of streamers, pulsed corona, etc.

The paper is organized as follows. In the first two sections, the PIC method is formulated, the interpolation of the gain/loss rate from the grid to the computational particles is discussed, and the implementation of a second-order-in-time algorithm is explained. Then, the particle-in-cell model is applied to two different problems. The first problem consists in an idealized electron avalanche propagating in a non-attaching gas. The rate constants and the velocity of electrons are given some specific functional forms that allow us to obtain a simple analytical solution. This problem is then used to validate the optimum interpolation of the gain/loss rate and to analyze the effect of the mass matrix formulation of the PIC model. The second problem, which is much more complex, is a realistic model of the propagation of a Trichel pulse between a sphere and a plate. No analytical solution can be obtained in this case and the results obtained from the PIC simulation will then be compared with those obtained from a FCT method.

2. THE CONTINUITY EQUATION

The one-dimensional partial differential equation governing the mass density of a chemical species in a gas discharge can be expressed as

$$\frac{\partial \rho}{\partial t} + \frac{\partial}{\partial x}(\rho v) = S(x, t), \tag{1}$$

where ρ is the mass density, v is the velocity, and S is the gain/loss rate of the mass density. This last term accounts for processes such as ionization, attachment, and recombination that result in a variation of the mass density. For simplicity, diffusion has been ignored in Eq. (1).

The mass density can be written as

$$\rho(x,t) = mN(x,t), \tag{2}$$

where m is the mass of the physical particles, which is constant, and $N(x,t)$ is the number density of particles, which usually changes by many orders of magnitude due to the physical processes indicated before.

In PIC simulations, physical particles are simulated by means of computational particles.A common solution adopted in PIC simulations to account for chemical reactions is to allow the mass of the computational particles to vary in time [17, 24]. To express this approach through continuous equations, it is convenient to rewrite Eq. (2) as the product of a density of *fictitious carriers*, $\mathcal{N}(x,t)$, whose number is conserved, and the mass of these carriers, $\mu(x,t)$, which changes continuously in time,

$$\rho(x,t) = \mu(x,t)\mathcal{N}(x,t). \tag{3}$$

The density of these fictitious carriers will therefore satisfy a homogeneous continuity equation

$$\frac{\partial \mathcal{N}}{\partial t} + \frac{\partial}{\partial x}(\mathcal{N}v) = 0, \tag{4}$$

while the equation governing the mass of carriers can be obtained by substituting Eq. (3) in (1),

$$\frac{d\mu}{dt} = S(x,t)/\mathcal{N}, \tag{5}$$

where d/dt represents the Lagrangian time derivative, $d/dt = \partial/\partial t + v\partial/\partial x$.

3. THE PARTICLE-IN-CELL MODEL

In PIC simulations, the mass density and the particle density are represented by approximated values on an array of grid points. The interaction between the different species is also calculated on the grid points. In contrast, the transport of mass is simulated by means of computational particles or *superparticles*. Superparticles can be regarded as finite-size clouds of physical particles, their position being the center of mass of the clouds and their velocities being the mean velocities of the clouds. The computational particles, labeled with the subscript p, will therefore be characterized with a mass μ_p, *a* position x_p, and a velocity v_p.

The mass and momentum density at the grid point x_g can written as [3]

$$\rho(x_g,t) = \frac{1}{H}\sum_p \mu_p W(|x_g - x_p|), \tag{6}$$

$$(\rho v)(x_g,t) = \frac{1}{H}\sum_p \mu_p v_p W(|x_g - x_p|), \tag{7}$$

where H is set to the grid spacing and W is the assignment function shape, with

$$\sum_g W(|x_g - x_p|) = 1. \tag{8}$$

Similarly, the number density of carriers at the grid points and the associated first velocity moment can be expressed as

$$\mathcal{N}(x_g, t) = \frac{1}{H} \sum_p W(|x_g - x_p|), \tag{9}$$

$$(\mathcal{N}v)(x_g, t) = \frac{1}{H} \sum_p v_p W(|x_g - x_p|). \tag{10}$$

These approximate solutions satisfy the homogeneous continuity equation for $\mathcal{N}$, Eq. (4), since differentiating Eq. (9) with respect to time leads to

$$\frac{\partial \mathcal{N}}{\partial t} = \frac{1}{H} \sum_p \frac{dx_p}{dt} W'(|x_g - x_p|) = -\frac{\partial}{\partial x}(\mathcal{N}v). \tag{11}$$

However, in fluid PIC simulation of gas discharges, the velocity of species at the grid points is entirely determined by the local electric field, which is in turn obtained from the charge density values on the grid. Therefore, in order to guarantee the internal coherence of the PIC model, the momentum density, as expressed by Eq. (7), is forced to satisfy

$$(\rho v)(x_g, t) = \rho(x_g, t) v(x_g, t). \tag{12}$$

In general, particle velocities should not be determined from the direct interpolation of the grid-defined values, since in that case Eq. (12) would not be satisfied.[2] Instead, a modified velocity, $u(x_g, t)$, is interpolated to the computational particles,

$$v_p = \sum_g u(x_g, t) W(|x_g - x_p|). \tag{13}$$

Substitution of this equation in (12) shows that this modified velocity can be obtained from the solution of

$$\sum_{g'} C^*_{g,g'} u(x_{g'}, t) = \rho(x_g, t) v(x_g, t), \tag{14}$$

where

$$C^*_{g,g'} = \frac{1}{H} \sum_p \mu_p W(|x_g - x_p|) W(|x_{g'} - x_p|) \tag{15}$$

is the *mass matrix* associated with the mass density.

[2] Grid-defined values of the particle velocities can be directly interpolated when a *nearest grid point* (NGP) interpolation is chosen as the assignment scheme.

The displacement of the computational particles can then be calculated by integrating its equation of motion

$$\frac{dx_p}{dt} = v_p. \tag{16}$$

3.1. *The Interpolation of the Gain/Loss Rate*

In gas discharges, the terms appearing in the gain/loss rate may have many different forms, depending on the type of reactions that participate in the discharge. However, for every species, these terms can be roughly classified into one of these two categories:

- Gain/loss rate terms that are independent of the mass density of the species, $S(x, t)$.
- Gain/loss rate terms that are proportional to the mass density of the species, that is,

$$S^*(x, t) = K(x, t)\rho(x, t).$$

In general, the proportionality constant $K(x, t)$, or the complete gain/loss rate in the first case, $S(x, t)$, depends on the mass density of the other species and on the electric field, which is obtained by solving Poisson's equation. Examples of reactions whose gain/loss rates are proportional to the mass density are, for the electrons, ionization, electron attachment to neutral molecules, and recombination between electrons and positive ions. In contrast, for positive and negative ions, ionization is an example of a reaction whose gain/loss rate is independent of the mass density of ions.

In this section, two different forms of interpolation of the gain/loss rates from the grid to the computational particles will be presented, according to the previous classification. The first form of interpolation can be applied to both categories. Indeed, this form of interpolation has also been applied in PIC models of chemically reacting fluid flows [24]. However, as will be shown below, the application of this type of interpolation to those gain/loss rates pertaining to the second category will always result in solutions with a worse accuracy. Since the evolution of transient gas discharges is governed by electron density, and the gain/loss rate of the electron density is proportional to itself, it is important to use the second form of interpolation whenever it applies.

3.1.1. Gain/loss rate terms independent of the mass density. As has been said previously, the mass of computational particles is not constant, but changes in time. The rate of variation of the mass of every computational particle is interpolated from the grid points using the same assignment function shape,

$$\frac{d\mu_p}{dt} = \sum_g s(x_g, t)W(|x_g - x_p|). \tag{17}$$

According to Eq. (5),

$$s(x_g, t) = \frac{S(x_g, t)}{\mathcal{N}(x_g, t)} \tag{18}$$

would seem to be the proper choice. However, substitution of Eqs. (6) and (7) in Eq. (1) shows that the rate of variation of the mass of computational particles should satisfy

$$\frac{1}{H}\sum_p \frac{d\mu_p}{dt} W(|x_g - x_p|) = S(x_g, t). \tag{19}$$

Taking into account (17), the above equation can be written as

$$\sum_{g'} C_{g,g'} s(x_{g'}, t) = S(x_g, t), \tag{20}$$

where

$$C_{g,g'} = \frac{1}{H} \sum_{p} W(|x_g - x_p|) W(|x_{g'} - x_p|) \tag{21}$$

is the analogous to the *mass matrix*. However, this mass matrix is not associated with the mass density but with the number density of computational particles. The rate of mass variation at the grid points, $s(x_g, t)$, should then be obtained by solving the system of linear equations (20). When the mass matrix formulation is not used and $s(x_g, t)$ is taken as expressed by Eq. (18), numerical diffusion of the gain/loss rate will appear between adjacent grid points.[3]

The mass matrix formulation must be used with care in the presence of a discontinuity that extends over very few cells. In such cases, the evaluation of the mass matrix across the discontinuity leads to unphysical oscillations of the interpolated quantity [6].

3.1.2. Gain/loss rate terms proportional to the mass density. In these cases, the rate of variation of the mass of carriers is also proportional to the mass of carriers itself, since according to Eq. (5),

$$\frac{d\mu}{dt} = \frac{S^*(x_g, t)}{\mathcal{N}(x_g, t)} = \frac{K(x, t)\rho(x, t)}{\mathcal{N}(x, t)} = K(x, t)\mu. \tag{22}$$

Therefore, when interpolating grid-defined values to the computational particle, only the proportionality constant $K(x, t)$ should be interpolated. The rate of variation of the mass of a computational particle can then be written as

$$\frac{d\mu_p}{dt} = \mu_p \sum_{g} k(x_g, t) W(|x_g - x_p|), \tag{23}$$

where $k(x_g, t)$ may differ from $K(x_g, t)$ to satisfy Eq. (19). Substitution of (23) in (19) gives

$$\sum_{g'} C^*_{g,g'} k(x_{g'}, t) = S^*(x_g, t) = K(x_g, t)\rho(x_g, t), \tag{24}$$

where $C^*_{g,g'}$ is the mass matrix of the PIC formulation. Therefore, as in the previous case, the value of $k(x_g, t)$ that is interpolated from the grid to the particles should be obtained from the solution of a system of linear equations.

Clearly, the mass matrix formulation would not be required in those cases where $K(x, t)$ is independent of the spatial coordinate, since

$$\sum_{g'} C^*_{g,g'} K(t) = K(t) \frac{1}{H} \sum_{p} \mu_p W(|x_g - x_p|) \sum_{g'} W(|x_{g'} - x_p|) = K(t)\rho(x, t). \tag{25}$$

[3] As in the case of velocity, Eq. (18) can be used with no numerical diffusion when a NGP interpolation is chosen for the assignment scheme.

In contrast, using the first type of interpolation, a constant value of K does not suffice to satisfy Eq. (20) since it is also required that $\rho(x,t)/\mathcal{N}(x,t)$ be independent of x. This is verified when the mass of all computational particles is identical, which is hardly found in PIC simulations of gas discharges.

There are several reasons why this type of interpolation should always be preferred. The first one is that the interpolated function, $K(x,t)$, will always be smoother than $K(x,t)\rho(x,t)/\mathcal{N}(x,t)$. This is so because the gain/loss rate is proportional to the mass density and, in gas discharges, the mass density is expected to vary exponentially in time with K. In the second place, this type of interpolation will never assign mass to those computational particles with zero initial mass. This property is consistent with the fact that these zero mass particles do not contribute to the grid values of the gain/loss rate. As a result, numerical diffusion of mass is prevented at propagating fronts, which are usually present in transient gas discharges. Finally, with this interpolation, the mass of particles is guaranteed to remain always positive, since it is $d(\ln \mu_p)/dt$, and not $d\mu_p/dt$, that has to be integrated in Eq. (23). The assignment of negative mass to computational particles usually has disastrous consequences in PIC simulations.

All these advantages together result in very accurate solutions, so that the mass matrix formulation is often not required. In constrast, when the other scheme of interpolation is used, the simulation will commonly produce worse results, unless the mass matrix formulation is included in the algorithm.

This type of interpolation can also be extended to those gain/loss rates that are proportional to an integer power of the density, $S^* = K(x,t)\rho(x,t)^n$. In such cases, only $K(x,t)\rho(x,t)^{n-1}$ should be interpolated from the grid to the computational particles.

3.2. *The Computational Algorithm*

In contrast with Ref. [17], the time integration scheme used in this paper is not implicit, that is, the continuity equation is successively integrated in time. Fully implicit plasma fluid codes are particularly efficient for calculating steady-state solutions, since implicit differencing eliminates stability constraints on the time step. In the work of Lapenta *et al.* [17], a PIC simulation of a DC glow discharge is performed. In this kind of electrical discharge, the solution is usually sought at the stationary state and therefore an implicit method of integration is certainly a right choice. Explicit methods have the advantage of being simpler and having a lower computational cost per time step, although the length of the time step is limited. Since our PIC formulation deals primarily with transient gas discharges that develop in very short times (tens of nanoseconds), an explicit method of integration that is second-order accurate in time (second-order Runge–Kutta method) has been preferred. A listing of the computational steps in a computational cycle follows:

1. The mass of computational particles is interpolated to the grid to obtain the mass densities of species (Eq. (6)) and the net electrical charge.
2. The electric field at the grid point is then determined by solving Poisson's equation.
3. The gain/loss rates, $S(x_g,t)$ and $S^*(x_g,t)$, and the velocities of species, $v(x_g,t)$, are evaluated at the grid points. Then the mass matrices, $C^*_{g,g'}$ and $C_{g,g'}$, are computed (Eqs. (15) and (21)) and the systems of equations (14), (20), and (24) is solved.
4. The grid values of $u(x_g,t)$, $s(x_g,t)$, and $k(x_g,t)$ are interpolated back to the particles to obtain $v_p = dx_p/dt$ and $d\mu_p/dt$.

5. Time is advanced by a half step, $\frac{1}{2}\Delta t$, and the particles' positions are updated to $x_p + \frac{1}{2}v_p\Delta t$. Then steps 1 to 4 are repeated, and the particles' velocities and the rate of mass variation of particles are evaluated at this intermediate step.

6. Finally, the particles' positions and the mass of particles are updated at a complete time step, Δt, using a second-order Runge–Kutta approximation,

$$x_p(t+\Delta t) = x_p(t) + \Delta t \left.\frac{dx_p}{dt}\right|_{(t+\frac{1}{2}\Delta t, x_p+\frac{1}{2}v_p\Delta t)}, \tag{26}$$

$$\mu_p(t+\Delta t) = \mu_p(t)\ \Delta t \left.\frac{d\mu_p}{dt}\right|_{(t+\frac{1}{2}\Delta t, x_p+\frac{1}{2}v_p\Delta t)}. \tag{27}$$

7. The computational cycle is restarted at $t + \Delta t$.

The same computational steps will be present if a higher order of integration in time is used, the only difference being that a greater number of intermediate steps will be required.

4. IDEALIZED ELECTRON AVALANCHE

This test problem is based on the continuity equations that govern a one-dimensional electron pulse propagating in a nonuniform electric field. As the electron pulse advances from the cathode to the anode, more electrons and positive ions are generated due to the ionization of the neutral molecules. The gas filling the space between the electrodes is assumed to be a non-attaching gas, so that no negative ions are generated during the development of the discharge. The continuity equations corresponding to this problem can be written as

$$\frac{\partial \rho_e}{\partial t} + \frac{\partial}{\partial x}(\rho_e v_e) = S_e^*(x,t), \tag{28}$$

$$\frac{\partial \rho_+}{\partial t} = S_+(x,t), \tag{29}$$

where ρ_e and ρ_+ are the mass densities of electrons and positive ions. The velocity of positive ions is set to zero, since it is several orders of magnitude smaller than the velocity of electrons, v_e. The gain/loss rates of mass density for electrons and positive ions are identical and proportional to the electrons' mass density,

$$S_e^*(x,t) = S_+(x,t) = K(x)\rho_e(x,t).$$

For simplicity, the effect of the space charge on the electric field has been ignored. Therefore, both the velocity of electrons and the rate constant, K, are assumed to be known functions of the spatial coordinate. Finally, diffusion of electrons and ions has also been ignored.

A simple analytical solution of Eqs. (28) and (29) can be obtained for the case when the electron velocity and the rate constant are related as

$$K(x) = c + \frac{dv_e}{dx}, \tag{30}$$

where c is a constant. In such a case, the continuity equation for electrons can be transformed into

$$\frac{d\rho_e}{dt} = \frac{\partial \rho_e}{\partial t} + v_e\frac{\partial \rho_e}{\partial x} = c\rho_e(x,t), \tag{31}$$

whose solution can be expressed as

$$\rho_e(x,t) = \rho_e(x_0,0)\exp(ct), \tag{32}$$

and x_0 is the starting position of an electron that arrives at the coordinate x after traveling a time t.

Once the mass density of electrons has been determined, the positive ion distribution can be easily obtained after performing a time integration of Eq. (29),

$$\rho_+(x,t) = K(x)\int_0^t \rho_e(x_0,0)\exp(ct)\,dt. \tag{33}$$

Setting the initial condition for electrons and ions to

$$\rho_e(x,0) = \begin{cases} 1, & \text{for } x_a < x < x_b, \\ 0, & \text{otherwise,} \end{cases} \qquad \rho_+(x,0) = 0, \text{ for all } x. \tag{34}$$

the analytical solution for the mass densities can be expressed as

$$\rho_e(x,t) = \begin{cases} \exp(ct), & \text{for } \Delta(x_b,x) < t < \Delta(x_a,x), \\ 0, & \text{otherwise.} \end{cases} \tag{35}$$

$$\rho_+(x,t) = \begin{cases} K(x)\dfrac{\exp(ct_{\min}) - \exp(ct_{\max})}{c}, & \text{for } t > \Delta(x_b,x), \\ 0, & \text{otherwise,} \end{cases} \tag{36}$$

where $\Delta(x',x)$ is the time taken for an electron to travel from x' to x; that is,

$$\Delta(x',x) = \int_{x'}^{x} \frac{dx}{v_e(x)}, \tag{37}$$

and $t_{\min} = \min[t, \Delta(x_a,x)]$, and $t_{\max} = \max[0, \Delta(x_b,x)]$.

4.1. *The PIC Simulation*

This test simulation has been primarily designed to make evident the effects of (a) using or not using the mass matrix formulation when interpolating the velocity of the species, (b) using or not using the mass matrix formulation when interpolating the gain/loss rates of the mass densities, and (c) using or not using the recommended type of interpolation for the gain/loss rates of the mass densities.

For the velocity, not using the mass matrix formulation means that the particle-interpolated grid velocity is directly the grid-defined velocity, that is, $u(x_g,t) = v(x_g,t)$. For the gain/loss rates, it means that either $s(x_g,t) = S(x_g,t)/\mathcal{N}(x_g,t)$ or $k(x_g) = K(x_g)$ is interpolated to the computational particles, depending on the choice made in (c).

The particle-in-cell simulation of this test has been run on a uniform grid with 101 nodes using a *cloud-in-cell* (CIC) assignment scheme. The initial pulse of electrons extends from $x_a = 0$ to $x_b = 40$, and, for convenience, the constant c has been taken as $c = \ln 10$ and the velocity of electrons as

$$v_e(x) = p + q\cos(ax), \tag{38}$$

with $p = 7, q = 4$ and $a = 3\pi/20$. The computations are initiated with 400 "superelectrons," that is, computational particles associated with the physical electrons. This number corresponds to an averaged density of 10 superelectrons per cell. The PIC simulation has been followed up to 10 units of time, and density profiles at the instant $t = 1$and $t = 10$ are presented in Fig. 1 for the electrons and in Fig. 2 for the ions. In these figures, the exact

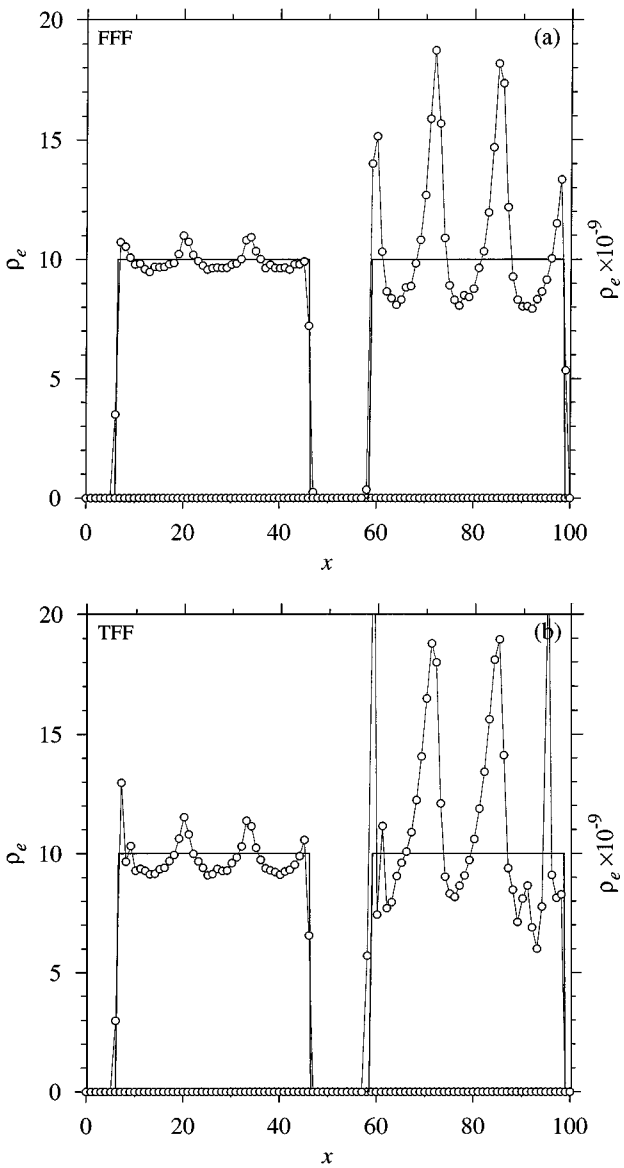

FIG. 1. Electron mass density at times $t = 1$ (left) and $t = 10$ (right) for an idealized electron avalanche. Thick solid line: exact solution; circles: PIC simulation. The PIC simulation has been carried out in different forms, as described by the three characters of the upper-left label. First character: the mass matrix formulation has been applied (T) or not applied (F) to the interpolation of velocity. Second character: the mass matrix formulation has been applied (T) or not applied (F) to the interpolation of the gain/loss rate. Third character: the proportionality of the gain/loss rate to density is exploited (T) or ignored (F).

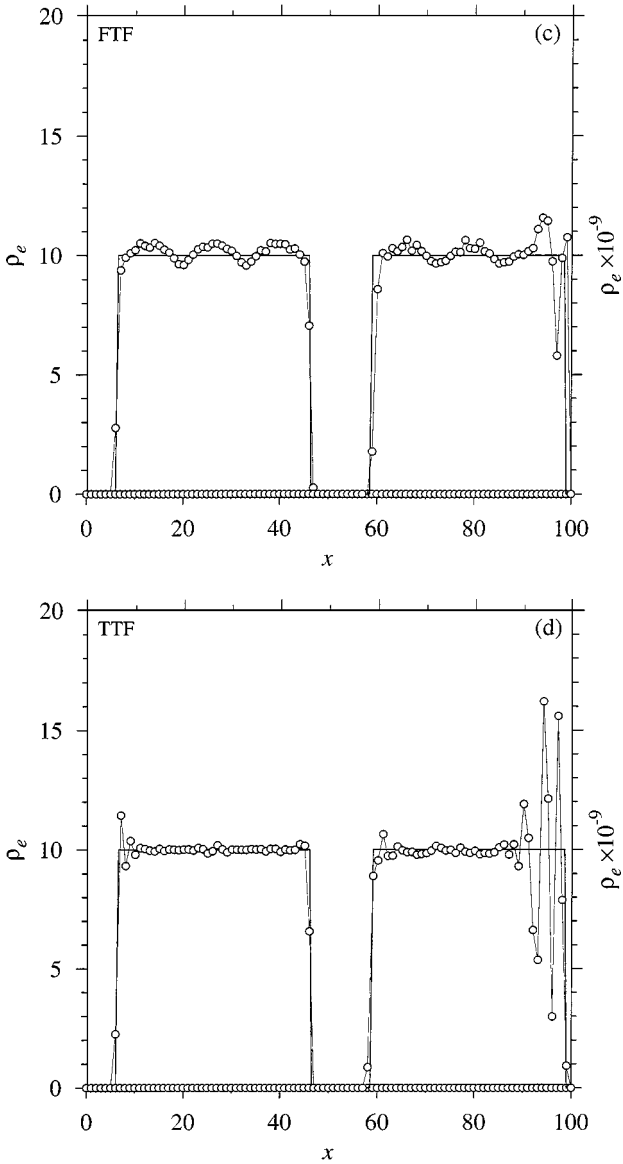

FIG. 1—*Continued*

solution is marked by a thick solid line, while the numerical simulation is represented with circles connected by a thin line. In each graph, the curves on the left (right) correspond to $t = 1$ ($t = 10$) and the density values must be read using the vertical axis on the left-hand side (right-hand side) of the graph. For the electrons (Fig. 1), the three-character label that has been inserted in the upper-left corner of the graphs indicates the options selected in the simulation. Each character may be either T (true) or F (false) and order of the characters is in correspondence with items (a), (b), and (c) listed at the beginning of this section. Hence, the label TFT in Fig. 1f means that the PIC simulation has been performed using the mass matrix formulation for the velocity but not for the gain/loss rate of mass density and that the interpolation of the gain/loss rate has been made as described in Section 3.1.2.

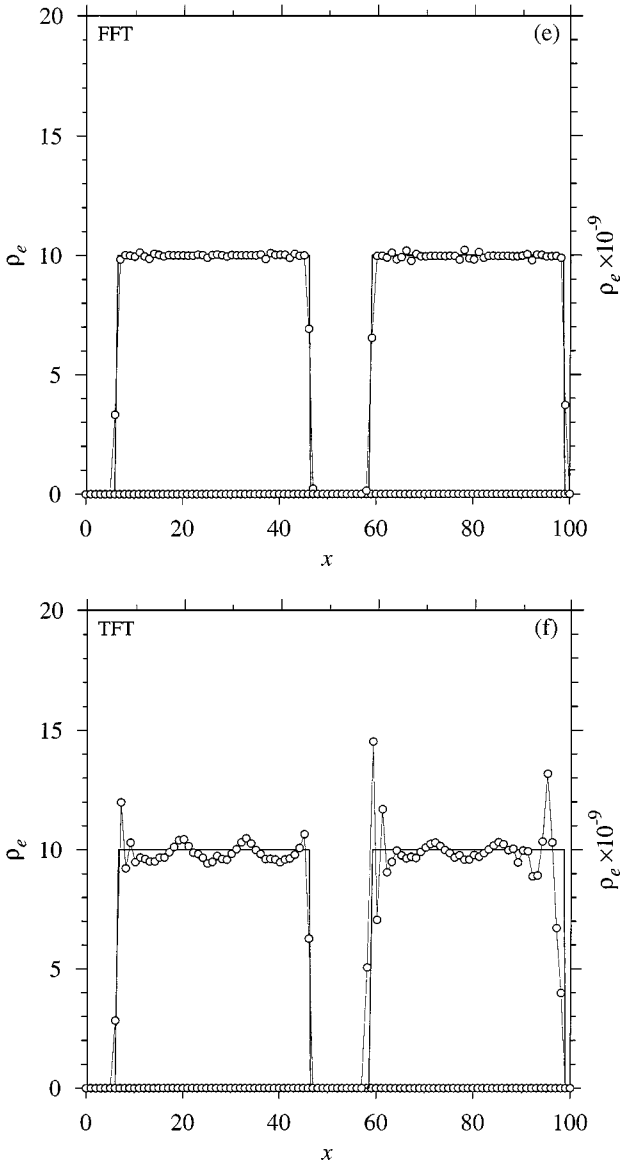

FIG. 1—*Continued*

According to the exact solution, the electron density will grow exponentially in time, increasing one order of magnitude for every unit of time, but keeping the initial rectangular distribution while propagating. Moreover, since the velocity of the pulse is identical at the limits x_a and x_b, the width of the pulse should be the same at all times.

Let us now compare the results of different PIC simulations among themselves and with the analytical solution. Figure 1a shows the electron density distribution for the case when the matrix formulation is not used and the interpolation of the gain/loss rate is performed without exploiting its proportionality with the mass density (Section 3.1.1). Clearly, the temporal evolution of the electron density is poorly reproduced: As soon as the simulation starts, the electron density exhibits a number of oscillations whose amplitudes increase with

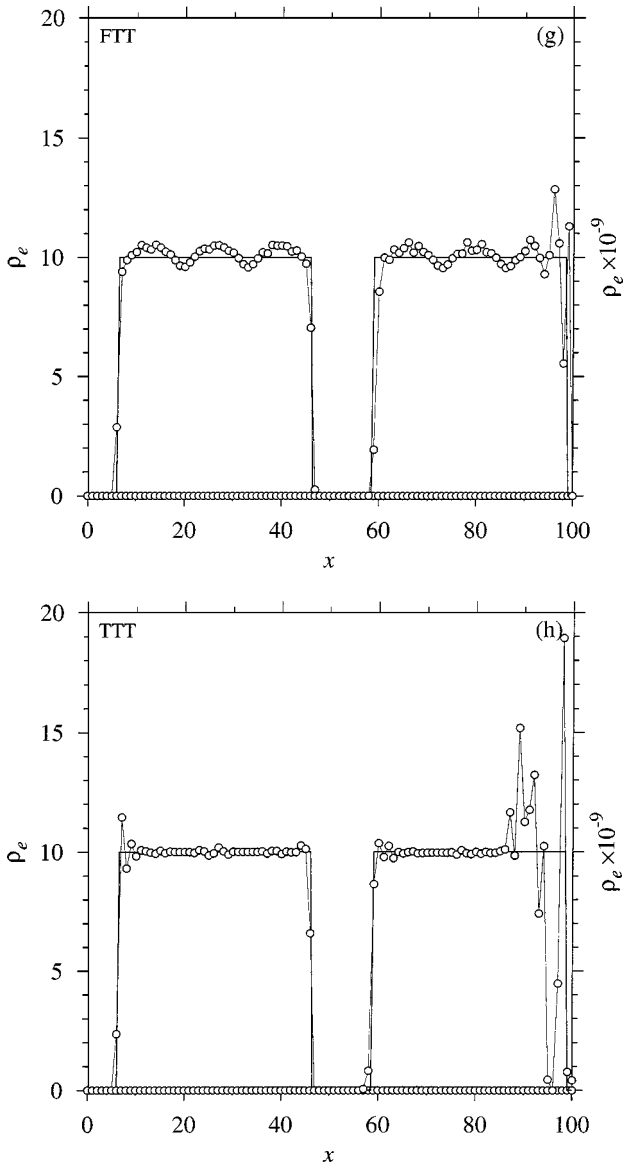

FIG. 1—*Continued*

time. These oscillations are practically in phase with the ratio $K(x)/v_e(x)$. This is because $K(x)\rho(x)/\mathcal{N}(x)$ is the rate of mass variation that is interpolated to the particles, and $\mathcal{N}(x)$ and $v_e(x)$ are phase-alike.

The results of this simulation are not essentially modified when the mass matrix formulation is applied to the electron velocity (Fig. 1b), but they do change when the mass matrix formulation is applied to the interpolation of the gain/loss rate (Fig. 1c). This fact shows that the interpolation errors affecting the gain/loss rate are much more important that those affecting the velocity. This is in turn a direct consequence of interpolating the gain/loss rate without taking advantage of its proportionality to the mass density. In this case, the rate of mass variation interpolated to the particles is proportional to the mass

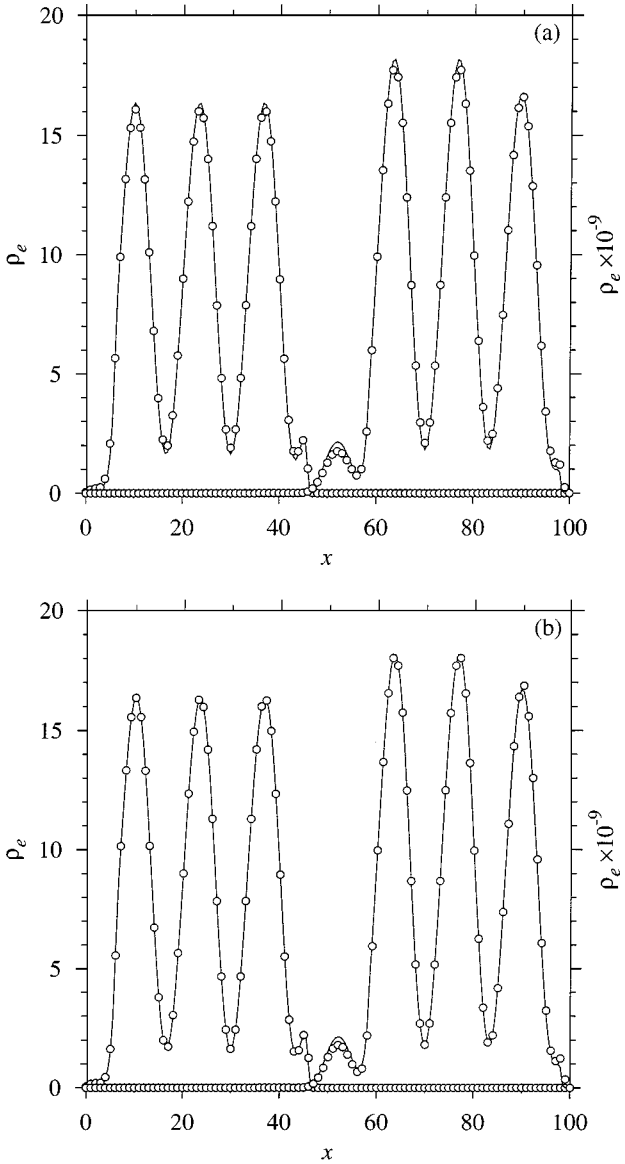

FIG. 2. Positive ion mass density at times $t = 1$ (left) and $t = 10$ (right) for the simulation of an idealized electron avalanche presented in Fig. 1e. Thick solid line: exact solution; circles: PIC simulation. (a) The mass matrix formulation has not been applied. (b) The mass matrix formulation has been applied.

density itself, which increases exponentially in time. Therefore, the interpolated quantity will be affected by large errors as time elapses. When the mass matrix formulation is used (Fig. 1c), interpolation errors of the gain/loss rate are suppressed and the results are more accurate. However, the application of the mass matrix formulation has an undesirable side effect: spurious oscillations appear at the limits of the electrons pulse, where the electron density is discontinuous. As has been mentioned earlier, these unphysical oscillations are commonly found when the mass matrix formulation is applied across a discontinuity that extends over very few cells [6].

Finally, when the mass matrix formulation is applied to both the velocity and the gain/loss rate interpolation (Fig. 1d), the numerical simulation is improved and matches the analytical solution more closely, except at the limits of the electron pulse, where the spurious oscillations become larger.

When the interpolation of the gain/loss rate is performed by taking advantage of its proportionality with the mass density (Section 3.1.2), the agreement between the PIC simulation and the exact solution is complete, even though the mass matrix formulation is not applied to the velocity and to the gain/loss rate interpolation (Fig. 1e). This result clearly shows that the interpolation of the gain/loss rate is now being performed much more accurately than in the previous cases.

Adding the mass matrix formulation to the velocity interpolation (Fig. 1f) or to the gain/loss rate interpolation (Fig. 1g) produces a worsening of the PIC simulation. The deterioration of the simulations is due to the loss of consistency between the forms in which $K(x)$ and $v_e(x)$ are interpolated from the grid to the particles, since there exists a close relation between the rate constant and the electron velocity (Eq. (30)). Moreover, the application of the mass matrix formulation gives rise to spurious oscillations at the edges of the square pulse, as has been previously observed.

However, when the mass matrix formulation is applied to both the interpolation of the velocity and the gain/loss rate (Fig. 1h), the internal consistency is recovered and the PIC simulation resembles more closely the exact solution, but unphysical oscillations persist at the limits of the square pulse, thus making this PIC simulation unacceptable.

There is a significant coincidence between the PIC simulations shown in Figs. 1c and 1g and Figs. 1d and 1h, respectively, even though they are all unsatisfactory. The only difference between these simulations is the type of interpolation used for the gain/loss rate, either without exploiting of its proportionality with the mass density (Figs. 1c and 1d) or by taking advantage of this proportionality (Figs. 1g and 1h). This agreement indicates that the choice of interpolation for the gain/loss rate is of secondary importance when the mass-matrix formulation is applied to the gain/loss rate, since interpolation errors of the gain/loss rate have been suppressed by the use of that formulation. However, the interpolation of the gain/loss rate without exploitation of its proportionality to density is not a valid option in simulations of gas discharges, since the application of the mass matrix formulation will always be required, and this will introduce necessarily spurious unphysical oscillations at the discontinuities. The presence of discontinuities and sharp gradients is not exceptional, but rather the rule, in real gas discharge problems.

In conclusion, the optimal PIC simulation is the one obtained by using the interpolation that exploits the proportionality to mass density of the gain/loss rate, and not applying the mass matrix formulation to the velocity and gain/loss rate (Fig. 1e), in order to avoid the unphysical oscillations associated with the presence of discontinuities. Only if we are certain that the grid resolution is high enough to resolve the density gradients, the mass matrix formulation for velocity and gain/loss rate may be added if an even more accurate solution is necessary.

Regarding the mass density of positive ions, the exact solution predicts an exponential growth in time modulated by the rate constant, which has a periodic character due to its relation with the electron velocity (Eq. (30)). In contrast to the case of electrons, the gain/loss rate for the mass of ions is independent of the mass density of ions. Therefore, in the PIC simulation, the rate of variation of the mass of the superions has to be evaluated as described in Section 3.1.1.

Figure 2 shows the results of the PIC simulation for the positive ions associated with the electron density shown in Fig. 1e. The mass matrix formulation for the interpolation of the gain/loss rate of ions has not been applied to the PIC simulation presented in Fig. 2a, but it has been applied to the simulation corresponding to Fig. 2b. There is fair agreement between the numerical results and the exact solutions in both simulations, although the simulation corresponding to Fig. 2b follows more closely the exact solution. The negligible effect of using the mass matrix formulation can be understood by looking carefully at the interpolated quantity, $S_+(x,t)/\mathcal{N}_+ = K(x)\rho_e(x,t)/\mathcal{N}_+$. Since the positive ion velocity has been set to zero, the computational particle density is constant in time (10 particles per cell). Moreover, the electron mass density is constant as well, as shown in Fig. 1e. Therefore, only the rate constant $K(x)$ is subjected to the mass matrix correction. This situation is somewhat similar to the case where the gain/loss rate of electrons was interpolated by taking advantage of its proportionality with the mass density. And, as in that case, the corrections introduced by the mass matrix formulation are negligible (cf. Figs. 1e and 1h).

Finally, Fig. 3 shows the superelectron density, $\mathcal{N}_e$, corresponding to the case presented in Fig. 1e. Care must be taken not to confuse $\mathcal{N}_e$ with the number density of electrons, which is proportional to the electron mass density. Instead, $\mathcal{N}_e$ is a density of computational particles. As in the previous graphs, the curve on the left (right) corresponds to the time $t = 1$ ($t = 10$). The strong oscillations exhibited by the density of superelectrons are associated with the spatial dependence of the electron velocity. At the minima, the density of computational particles can be as low as three superelectrons per cell. However, since the mass of every superelectron is different, a constant electron density distribution may be accurately represented by a strongly oscillating superelectron density. The weak fluctuations that can be noticed in the electron density (see Fig. 1e) are associated with these minima of the superelectron density.

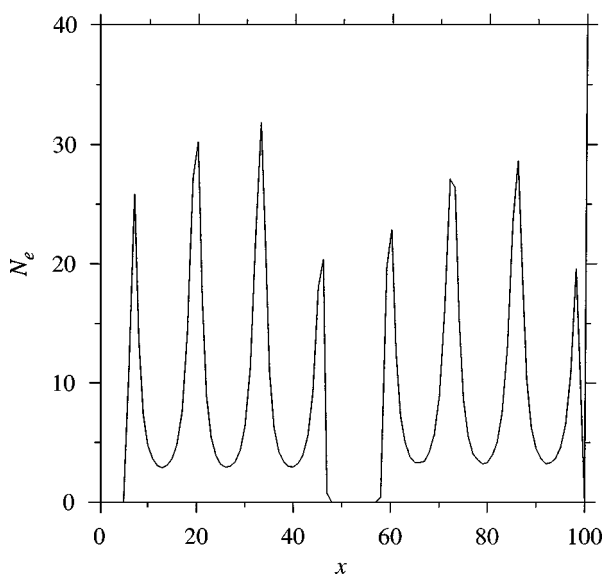

FIG. 3. Superelectron density at times $t = 1$ (left) and $t = 10$ (right) for the simulation of an idealized electron avalanche presented in Fig. 1e.

5. DEVELOPMENT OF A TRICHEL PULSE

The problem of a Trichel pulse propagating in low-pressure oxygen (50 Torr) has been investigated by Morrow [21] using an explicit flux-corrected transport (FCT) algorithm and other techniques described by Morrow and Cram [23]. Here, this problem will be used to check the suitability of the PIC model to simulate real gas discharges.

The Trichel pulse is assumed to develop between a sphere of radius $R = 5$ mm and an infinite plane at a distance $d = 20$ mm apart. The sphere is subjected to a high negative voltage, $V = -2900$ V, while the plane is grounded. The discharge is modeled as a cylindrical channel of radius 4 mm with a uniform radial distribution and a variable axial distribution of charge.

The one-dimensional continuity equations along the axis of symmetry, x, can be written as

$$\frac{\partial N_e}{\partial t} + \frac{\partial}{\partial x}(N_e v_e) = \alpha |v_e| N_e - \eta |v_e| N_e - \beta N_+ N_e, \tag{39}$$

$$\frac{\partial N_+}{\partial t} + \frac{\partial}{\partial x}(v_+ N_+) = \alpha |v_e| N_e - \beta N_e N_+ - \beta N_- N_+, \tag{40}$$

$$\frac{\partial N_-}{\partial t} + \frac{\partial}{\partial x}(v_- N_-) = \eta |v_e| N_e - \beta N_+ N_-, \tag{41}$$

where N is the number density, α, β, and η are the ionization, recombination, and attachment coefficients, and the subscripts e, $+$, and $-$ refer to electrons, positive ions, and negative ions respectively. Similarly to the previous simulation, electron diffusion has been omitted in Eq. (39). The reader is referred to the work of Morrow [21] for a detailed description of the transport coefficients used in the simulation.

Most of the transport coefficients depend on the electric field. The electric field along the x-axis is obtained as the superposition of the Laplacian electric field, and the space-charge field due to the discharge channel. The Laplacian electric field is obtained by the well-known method of images. The space-charge electric field, with homogeneous boundary conditions at the electrodes, is obtained by the method of disks. Basically, the method of disks assumes that the discharge channel may by discretized in a number of thin disks with uniform charge density. The contribution of disks to the space-charge electric field is then obtained by images as well.

The boundary conditions for the electrons and ions are

$$N_-(0, t) = 0, \tag{42}$$

$$N_+(d, t) = 0, \tag{43}$$

$$N_e(0, t) = N_e^p + N_e^i, \tag{44}$$

where N_e^p and N_e^i are the numbers of secondary electrons released at the cathode by the impacts of photons and ions, respectively. Denoting by γ_p and γ_i the efficiency factors of these processes, the number of secondary electrons can be written as

$$N_e^p(0, t) = \frac{\gamma_p}{|v_e(0, t)|} \phi(0, t), \tag{45}$$

$$N_e^i(0, t) = \frac{\gamma_i}{|v_e(0, t)|} N_+(0, t) |v_+(0, t)|, \tag{46}$$

where ϕ is the number of photons hitting a unit surface of the cathode in a unit time [21].

5.1. *The PIC Simulation*

In this section, we explain different aspects of the numerical implementation of this PIC simulation. The assignment scheme and its influence on the stability of the simulation is first discussed. Then, some details regarding the computational grid used in the simulation are given. Finally, the interpolation of the gain/loss rate terms of Eqs. (39)–(41) from the grid to the particles and the implementation of the physical boundaries are described.

5.1.1. The assignment scheme. In the test model simulation presented in Section 3, the electric field at the grid points and, therefore, the particle velocity were prescribed externally through Eq. (38). In the simulation of the Trichel pulse, in contrast, the electric field at the grid points is obtained from the grid-defined values of the particle densities. The method of disks is numerically implemented by means of an influence matrix operator [22], whose product with the grid-defined charge density gives the space charge-field. Once the total electric field (Laplacian plus space-charge electric field) is determined, the particle velocities are obtained from constitutive relations based on experimental data.

This difference has important consequences on the assignment scheme that may be used in the PIC simulation. In the test model, both the velocity of computational particles and the gain/loss rates were interpolated from the grid to particles using a CIC assignment scheme. This type of PIC simulation is classified as "momentum-conserving" [14]. However, this assignment scheme is unstable when it is applied to the numerical simulation of the Trichel pulse. The instability cannot be eliminated by shortening the time step or increasing the number of grid points and/or the number of computational particles. At best, these resorts can only delay the onset of the instability by a few nanoseconds. An example of this instability is presented in Fig. 4 (cf. Fig. 8d) for the electron density at $t = 60$ ns.

In contrast, the PIC simulation becomes stable when an "energy-conserving" scheme is used instead. In this assignment scheme, the electric field is evaluated directly at the

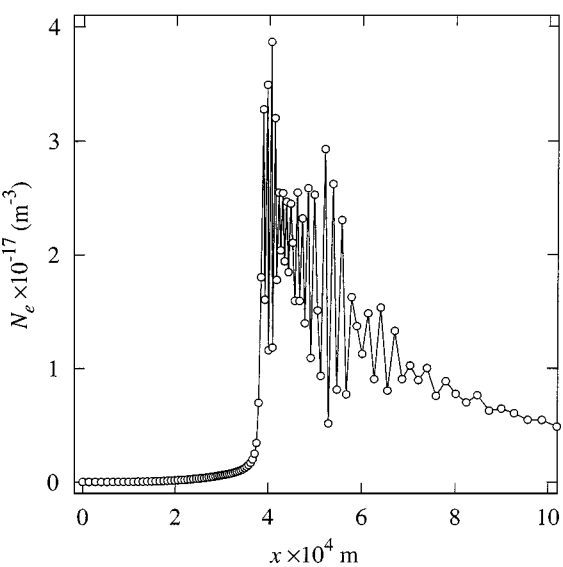

FIG. 4. Numerical instability of the PIC simulation of a Trichel pulse when a momentum-conserving scheme is used. The electron density at $t = 60$ ns is shown in the figure.

points $x_{g+1/2}$, lying midway between the grid points x_g and x_{g+1}. Then, the velocities of all computational particles inside the interval $[x_g, x_{g+1}]$ are given an identical value: the particle velocity corresponding to the electric field at $x_{g+1/2}$. Clearly, this particle velocity interpolation is equivalent to a *nearest grid point* (NGP) interpolation from a grid whose grid points are located at the cell boundaries of the original grid. In contrast, the interpolation of the gain/loss rates from the grid to the superparticles and the interpolation of the mass of computational particles to the grid will still be performed according to the standard CIC interpolation. The resulting scheme is therefore a mixed CIC/NGP assignment scheme.

In the Appendix, the stability of momentum- and energy-conserving schemes for a problem simpler than but closely related to the Trichel pulse problem is analyzed.

5.1.2. The computational grid. The PIC simulation has been run on a nonuniform grid with 181 nodes identical to the one described by Morrow [21]. The grid has a very fine resolution in the region where the electric field is very weak, $3 \times 10^{-4} \leq x \leq 4.5 \times 10^{-4}$ m, and becomes coarser as it approaches the cathode and the anode. For computational efficiency, the physical grid is mapped into a natural grid [4], where the separation between nodes is unity,

$$x_g = g, \quad g = 0, \ldots, 180.$$

5.1.3. The simulation in the bulk. Since Eqs. (39)–(41) are written in terms of the number density instead of the mass density, the computational particles in the PIC simulation will not be characterized by its mass, μ_p, but by the number of physical particles, $\bar{\mu}_p$, associated with the computational particle. Both quantities are related as

$$\bar{\mu}_p = \frac{\mu_p}{m},$$

where m is the mass of the physical particle. Of course, the PIC model described in Section 3 is equally valid in the present case, provided that μ_p is replaced by $\bar{\mu}_p$ everywhere.

The gain/loss rate of the number density of electrons (see Eq. (39)) is proportional to the number density of electrons itself. Therefore, the rate of variation of $\bar{\mu}_p$ for superelectrons, $\bar{\mu}_p^e$, should be evaluated according to the procedure described in Section 3.1.2,

$$\frac{d\bar{\mu}_p^e}{dt} = \bar{\mu}_p^e \sum_g s_e^*(x_g, t) W\left(\left|x_g - x_p^e\right|\right), \tag{47}$$

where x_p^e is the position of the superelectron and s_e^* is obtained by solving the following system of linear equation:

$$\sum_{g'} C_{g,g'}^{e,*} s_e^*(x_{g'}, t) = [\alpha|v_e|N_e - \eta|v_e|N_e - \beta N_+ N_e]_{x_g,t}. \tag{48}$$

If the mass matrix formulation is not used, then s_e^* is set to

$$s_e^*(x_g, t) = [\alpha|v_e| - \eta|v_e| - \beta N_+]_{x_g,t}.$$

For positive and negative ions, however, the gain/loss rates contain terms that are proportional and non-proportional to the respective number densities of ions (see Eqs. (40) and

(41)). In these cases, the rate of variation of $\bar{\mu}_p$ will have two distinct contributions that should be evaluated separately. For the positive ions, for example, we have

$$\frac{d\bar{\mu}_p^+}{dt} = \sum_g s_+(x_g, t) W(|x_g - x_p^+|) + \bar{\mu}_p^+ \sum_g s_+^*(x_g, t) W(|x_g - x_p^+|), \tag{49}$$

where x_p^+ is now the position of the supercation and s_+ and s_+^* are obtained by solving the following systems of linear equations:

$$\sum_{g'} C_{g,g'}^+ s_+(x_{g'}, t) = [\alpha |v_e| N_e]_{x_g,t}, \tag{50}$$

$$\sum_{g'} C_{g,g'}^{+,*} s_+^*(x_{g'}, t) = [-\beta N_e N_+ - \beta N_- N_+]_{x_g,t}\,. \tag{51}$$

If the mass matrix formulation is not used, s_+ and s_+^* are given the following values:

$$s_+(x_g, t) = [\alpha |v_e| N_e / \mathcal{N}_+]_{x_g,t}, \tag{52}$$

$$s_+^*(x_g, t) = [-\beta (N_e + N_-)]_{x_g,t}. \tag{53}$$

A set of similar equations can be also written for the negative ions.

The mobility of electrons is several orders of magnitude greater than the mobility of ions. Moreover, the drift of electrons and positive ions occurs in opposite directions. These two facts must be taken into account to avoid the situation where the superelectrons, as they drift to the anode, enter a cell completely void of supercations and/or superanions. If that happens, the gain/loss rate of the ion densities at the grid point cannot be returned to the computational particles, since they will be absent in the cell. Therefore, as the electron head moves towards the anode, new superions with initial values $\bar{\mu}_p^+ = 0$ and $\bar{\mu}_p^- = 0$, have to be created. In the present simulation, superions are checked to exist as far as one cell ahead from the most advanced superelectron. In their absence, new superions are introduced to fill the void region with a density of 15 computational particles per cell.

5.1.4. Boundary–particle interaction. Physical boundaries are located at the cathode and at the anode, to which correspond the grid points x_0 and x_{180}, respectively. These physical boundaries may interact with the computational particles in three different forms, depending on the type of particles we are considering. Basically, the electrodes may behave as *absorbing*, *repelling*, and/or *injecting* boundaries.

Absorbing boundaries are the cathode for the positive ions and the anode for the negative ions and the electrons. This type of boundary is implemented by using two additional grid points beyond the original grid: $x_{-1} = -1$ and $x_{181} = 181$. Computational particles are not removed from the simulation until they cross these extended limits. Meanwhile, the super-cations located between the grid points x_{-1} and x_0 will still contribute to the positive ion density at the cathode and, correspondingly, the superanions and superelectrons between x_{180} and x_{181} will contribute to the negative ion density and electron density at the anode respectively. Since superparticles are absorbed progressively, there will not be sudden jumps in charge density that may cause unwanted fluctuations in the particle density. The velocity of these computational particles is evaluated from the electric field at the midpoints

$x_{-1+1/2}$ and $x_{180+1/2}$, which is linearly extrapolated from the two nearest midpoints in the grid.

Repelling boundaries are the cathode for the negative ions and the anode for the positive ions. This kind of boundary–particle interaction corresponds to the boundary conditions (42)–(43) and is implemented by excluding super-anions and super-cations from the grid intervals $[x_0, x_1)$ and $(x_{179}, x_{180}]$, respectively. Since the drift direction of negative ions is toward the anode, care must be taken to avoid a situation where the first grid cells become empty of superanions. This is accomplished by introducing new computational particles of this type, with a density of 15 particles per cell, in the void region to the right of the grid point x_1 . Similarly to the process of particle creation in the bulk, these new computational particles are created with $\bar{\mu}_p^- = 0$. At the anode, similar care must be taken with positive ions and, when necessary, new supercations should be introduced in the void region to the left of the grid point x_{179} .

Finally, the cathode also behaves as an injecting boundary for electrons, as expressed by the boundary condition (44). Taking into account Eqs. (45) and (46), this boundary condition fixes the rate at which secondary electrons are being introduced into the system from the cathode, that is, $|v_e(0,t)|N_e(0,t)$. Therefore, this boundary condition is implemented as a gain/loss rate for the number density of electrons at the first grid point. The rate of variation of $\bar{\mu}_p^e$ in the interval $[x_{-1}, x_1)$ is obtained as

$$\frac{d\bar{\mu}_p^e}{dt} = s_e'(x_0,t)W\left(\left|x_0 - x_p^e\right|\right) + \bar{\mu}_p^e s_e^*(x_1,t)W\left(\left|x_1 - x_p^e\right|\right), \tag{54}$$

where $s_e'(x_0,t)$ is the gain/loss rate associated with the boundary condition at the cathode,

$$s_e'(x_0,t) = \left[\frac{|v_e|N_e/(H/2)}{\mathcal{N}_e}\right]_{x_0,t}, \tag{55}$$

and $s_e^*(x_1,t)$ is the gain/loss rate due to the chemical reactions occurring in the first grid point in the bulk.

5.2. *Numerical Results*

In this section, the results of the PIC simulation will be analyzed and compared with those obtained using a FCT method. The FCT algorithm implemented here is basically identical to the one used by Morrow [21], that is, the Phoenical "low-phase error" Shasta algorithm of Boris and Book [2] complemented with Zalesak's peak preserver [27]. The time integration in both simulations has been performed by a second-order Runge–Kutta method with variable time step. The time step is adjusted to satisfy that $\Delta t < \Delta t_{\max} = H/2v_{\max}$, where $v_{\max}$ is the maximum value of the velocity at the grid points. This is in essence the Courant–Friedicks–Lewis condition for the stability of the numerical scheme. Both in the FCT and in the PIC simulation, the maximum size of the time step has been limited to $0.75\Delta t_{\max}$.

The PIC simulation starts at time $t = 0$ with the release of 400 seed electrons near the cathode. These seed electrons are represented by 309 computational particules (super-electrons) distributed along the first 21 cells. The electron density profile corresponding to these computational particles is a narrow Gaussian distribution with peak density of $1.52 \times 10^{11}\mathrm{m}^{-3}$ whose center is at a distance $x = 55\,\mu\mathrm{m}$ apart from the cathode. The

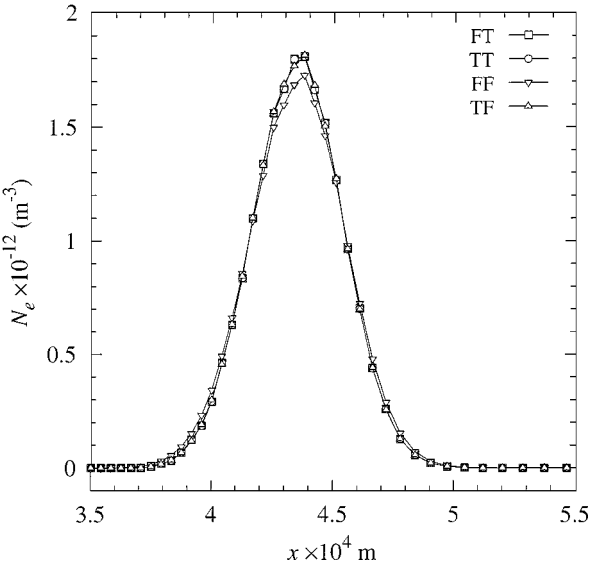

FIG. 5. Electron density in the early stages of the Trichel pulse simulation ($t = 1$ ns). The PIC simulation has been carried out in different forms, as described by the two characters in the upper-left label. First character: the mass matrix formulation has been applied (T) or not applied (F) to the interpolation of the gain/loss rate. Second character: the proportionality with density of the gain/loss rate is exploited (T) or ignored (F).

simulation has been followed during the first 213 ns, since this interval is long enough to observe the four different phases of the Trichel pulse defined by Morrow.

Let us first discuss the effect of applying or not applying the mass matrix formulation and exploiting or ignoring the proportionality to density of some of the terms appearing in the gain/loss rates. As before, a label of two characters will be used inside the plots to discern among the different PIC simulations. The first character of the label refers to the application of the mass matrix formulation (T: true, F: false) while the second indicates if the simulation has taken advantage of the proportionality to density of some of the terms of the gain/loss rates (T: true, F: false).

Figure 5 shows the electron density at $t = 1$ ns, after the PIC simulation has been run for 241 temporal steps. At this early stage, the initial electron distribution has drifted 375 μm towards the cathode and has already experienced some amplification. Comparing the four different simulations, we observe that, as in the model test of the electron avalanche, the mass matrix formulation has very little influence when the proportionality of the gain/loss rate to the mass density is used (FT and TT). In contrast, when this proportionality is ignored, the mass matrix correction is necessary in order to obtain an accurate solution (TF).

Since electrons are drifting in a highly non-uniform decreasing electric field, the electron distribution tends to collapse in to a delta function. Therefore, sooner or later, all the computational particles will be spread along a distance shorter than the width of a single cell. At that moment, the initial Gaussian distribution will only be defined by two or three grid points, depending on whether the packet of particles is exactly bounded by two grid points or is placed inside a cell. This configuration can be observed in Fig. 6a, corresponding to $t = 10$ ns. The agreement and the differences among the four PIC simulations

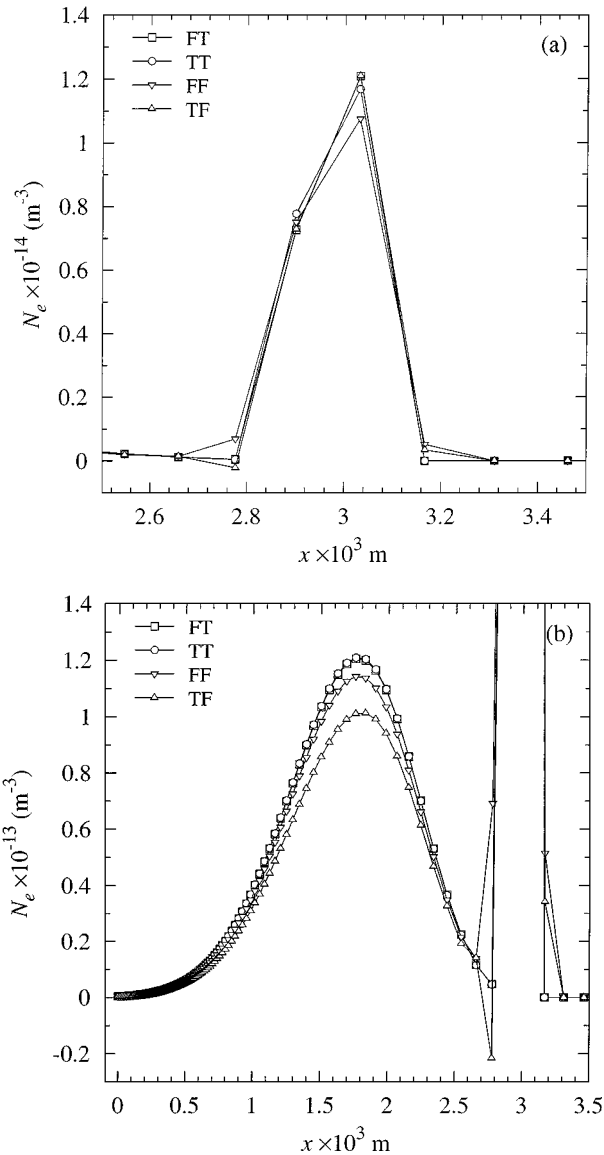

FIG. 6. Electron density in the early stages of the Trichel pulse simulation ($t = 10$ ns). (a) Detailed view of the electron avalanche head. (b) Detailed view of the secondary electrons released at the cathode. The PIC simulation has been carried out in different forms, as described by the two characters in the upper-left label. First character: the mass matrix formulation has been applied (T) or not applied (F) to the interpolation of the gain/loss rate. Second character: the proportionality of the gain/loss rate to density is exploited (T) or ignored (F).

are practically unchanged with respect to the earlier time $t = 1$ ns. However, a new aspect of the simulation now appears: the use of the mass matrix formulation when the gain/loss rate has been interpolated without exploiting its proportionality with density (TF) has introduced a spurious fluctuation behind the electron pulse. At later times, this fluctuation may appear either behind, ahead of, or both behind and ahead of the electron pulse.

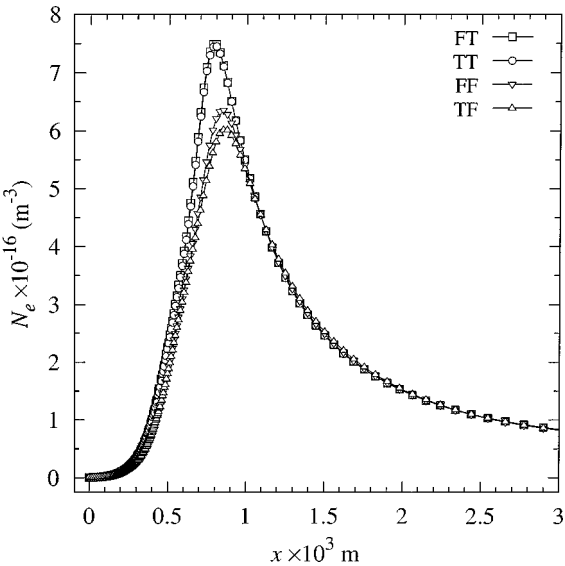

FIG. 7. Electron density distribution in the Trichel pulse at $t = 43$ ns. The PIC simulation has been carried out in different forms, as described by the two characters in the upper-left label. First character: the mass matrix formulation has been applied (T) or not applied (F) to the interpolation of the gain/loss rate. Second character: the proportionality with density of the gain/loss rate is exploited (T) or ignored (F).

At this stage of the simulation, secondary electrons at the cathode are mainly released by the impact of the photons generated by ionization in the bulk. The number of impacts is proportional to the rate of ionization in the bulk and therefore depends on the electric field strength. The existence of a fluctuation behind the electron pulse, where the particle density becomes "negative" and the electric field is stronger, will contribute to a noticeable decrease in the number of secondary electrons released by the cathode. This effect can be appreciated in Fig. 6b, where a detailed view of the density of secondary electrons at $t = 10$ ns is presented. The presence of these spurious oscillation deteriorates the PIC simulation, affecting it irreversibly at all later times. As an example, Fig. 7 shows the electron density distribution at the instant $t = 43$ ns. The results of the PIC simulations where the dependence of the gain/loss rate on the density have been exploited (FT and TT) are practically coincident. In contrast, the results of the other PIC simulations show a clear disagreement in the peak value of the electron density, which the application of the mass matrix formulation is unable to suppress.

Finally, Fig. 8 show the electric field distribution and the densities of electrons, positive ions and negative ions as the Trichel pulse develops. In these figures, only one of the four PIC simulations is presented: the one where the proportionality of the gain/loss rate with the mass density is used and the mass matrix formulation is not applied (FT). This PIC simulation is practically coincident at all times with the one where the mass matrix formulation is used (TT). However, some discrepancies have always been observed with the other two PIC simulations.

The results of PIC simulation (markers) show an excellent agreement with the predictions of the FCT simulation (solid line). Some minor fluctuations can be noticed in the electric field distribution (Fig. 8c) and in the electron density (Fig. 8d). These

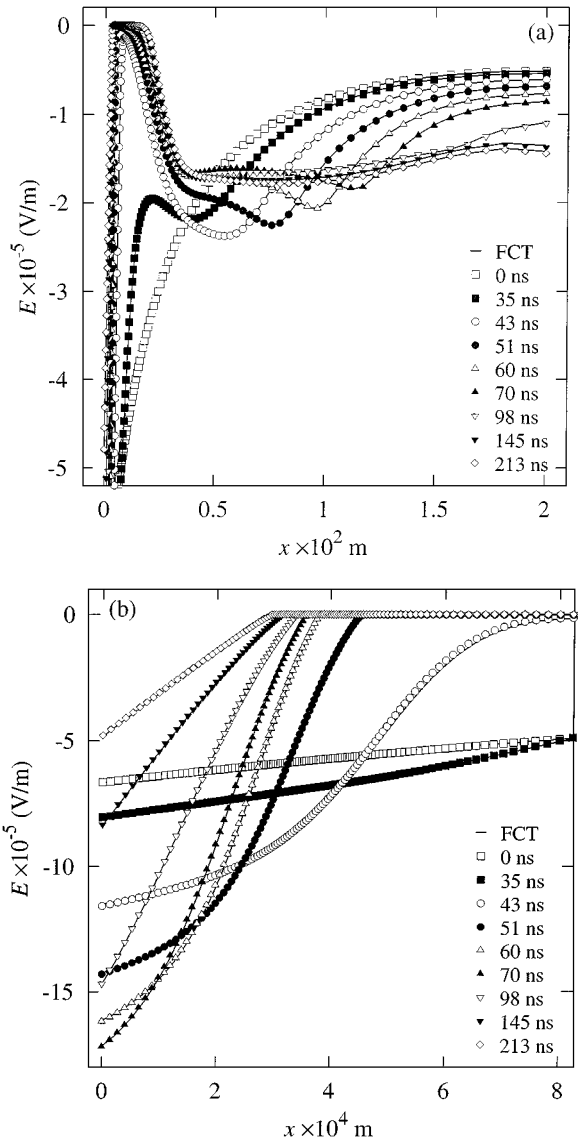

FIG. 8. Time evolution of the Trichel pulse. Markers: PIC simulation. Solid line: FCT simulation. (a) Electric field distribution for the complete gap. (b) Detailed view of the electric field in the vicinity of the cathode. (c) Detailed view of the low-field region. (d) Electron density distribution in the vicinity of the cathode. (e) Positive ion density distribution in the vicinity of the cathode. (f) Negative ion density distribution in the vicinity of the cathode.

fluctuations occur at the location where the plasma regions begin. At that point, super-electrons injected from the cathode tend to accumulate, due to the sharp gradient on the electric field, and are slowly evacuated through the plasma region. However, this small fluctuation is very localized and does not tend to amplify in time. On the other hand, the positive ion density (Fig. 8e) obtained by means of the FCT simulation shows the characteristic staircase formation of this numerical technique [15], which is absent in the PIC simulation.

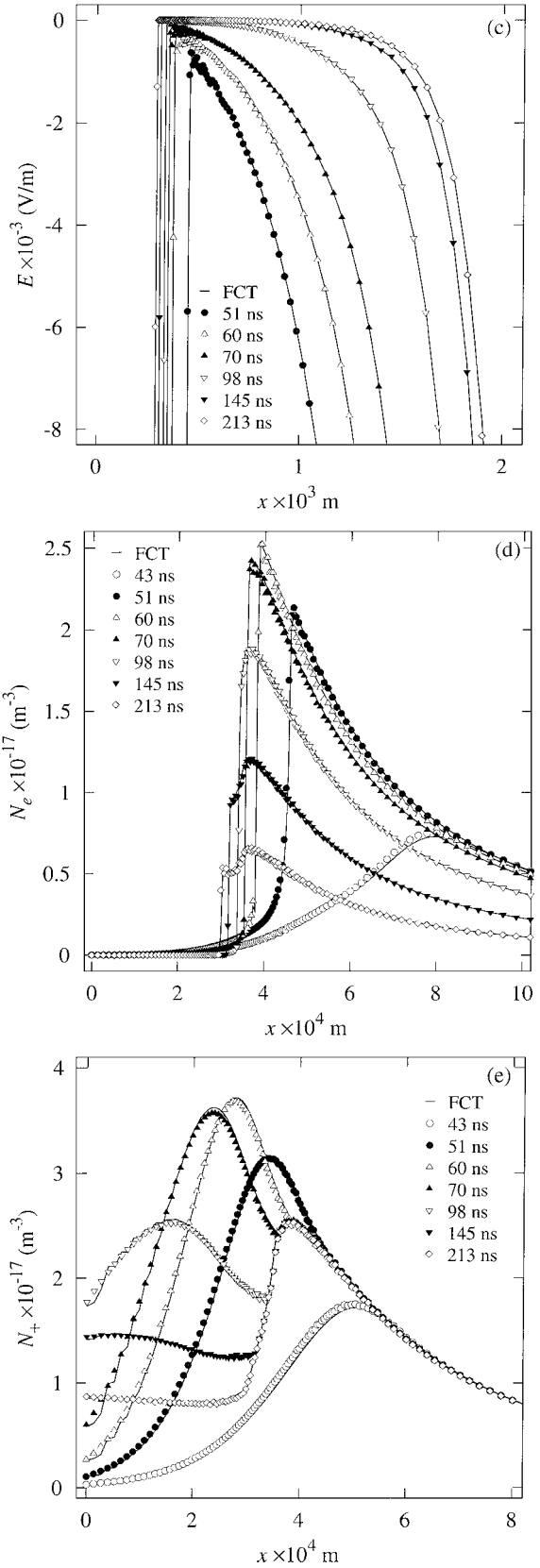

FIG. 8—*Continued*

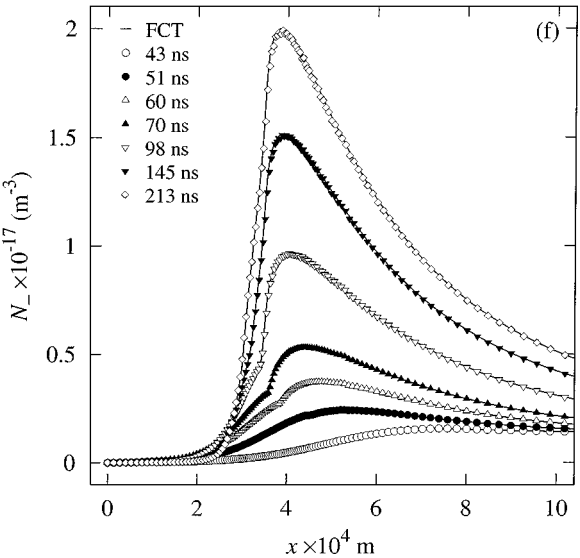

FIG. 8—*Continued*

6. CONCLUSIONS

The application of a PIC fluid model to the numerical simulation of transient gas discharges has shown the ability of the method to deal satisfactorily with fast time variations and sharp gradients.

Two different tests are performed. First, the numerical scheme is checked with the problem of an idealized electron avalanche in a non-attaching gas. This problem possesses an analytical solution where the electron density grows exponentially in time while propagating. Then, the propagation of a Trichel pulse in oxygen is simulated. This is a particularly difficult test since it combines the presence of very sharp gradients of the particle densities and the existence of plasma region where the electric field almost vanishes. The results of the PIC simulation are compared with those obtained from the application of a explicit FCT algorithm. The agreement between both methods is remarkable.

These tests are used to investigate the effects of the application of the mass matrix formulation to the model, and to analyze the optimum interpolation of the gain/loss rate of mass (or particle) density from the grid to the computational particles. In particular, the analysis shows that more accurate results are always obtained when the proportionality of the gain/loss rate to mass density is exploited. Therefore, the use of a unique interpolation for all types of gain/loss rates, where this proportionality is not used, is completely discouraged. Analogously, the application of the mass matrix formulation may have severe side effects in PIC simulations, since spurious fluctuations may originate in those regions where the mass density exhibits sharps gradients. Since the presence of sharp gradients is a common feature in most of the transient discharges, the use of the mass matrix simulation is only recommended upon the verification that the numerical solution without mass matrix lacks discontinuities extending over a few grid points. However, in numerical tests, the application of the mass matrix formulation was unnecessary when the proportionality with the mass density of the gain/loss rates was taken into account, since in this case the corrections introduced by using the mass matrix formulation were small.

The next step of this study will be to extend this numerical method to the case of multidimensional geometry since, from the conceptual point of view, this extension poses no additional complications, contrary to 2D and 3D flux-corrected-transport schemes.

APPENDIX: STABILITY ANALYSIS

Momentum-conserving schemes interpolate the values of both the mass density and the electric field at the grid points to the computational particles. In contrast, energy conserving schemes interpolate the grid-defined values of the mass density and the electric field values at the cell boundaries into the computational particles. Moreover, the order of the interpolation for the electric field must be one order lower than the one used for the mass density.

The instability of the momentum-conserving scheme observed in PIC simulation of the Trichel pulse can be understood as a particular case of the well-known "finite-grid instability" or "ringing instability," as it is termed in the fields of plasma kinetic simulation [5, 16, 18] and fluid PIC simulation [3], respectively. This instability is caused by the spurious coupling of the Fourier modes resolved by the grid and their "alias." The stability analysis that we present below follows a line of reasoning analogous to those given in [3, 5, 14].

Let us consider a simplified system consisting of an infinitely long gas discharge channel where the electrons are the only mobile carriers. These electrons drift across a uniform background of static positive ions with density N_0 because of the electric field. Since the origin of the instability is linked to the transport of charge and not to its generation, the evolution of the electron density will be studied by using the homogeneous continuity equation

$$\frac{\partial N}{\partial t} + \frac{\partial}{\partial x}(Nv) = 0, \tag{56}$$

where x is the axis of the discharge, $N(x)$ is the electron density, and $v(x) = -bE(x)$ is the drift velocity of electrons with constant mobility b. Similarly to the Trichel pulse simulation, the total electric field, $E(x)$, is obtained as the superposition of a Laplacian electric field of constant value, E_0, and the space charge field due to the discharge channel, $E'(x)$. The space charge electric field may be found using the method of disks. By proceeding in this way, this electric field is obtained as the convolution of a certain function, $F(x - x')$, with the charge density. This function is analogous to Green's function for the electrical potential, and is numerically implemented as an influence-matrix operator [22].

Equation (56) possesses a trivial equilibrium solution where the electron density is constant and equal to the positive ion density, N_0, and the total electric field is the Laplacian electric field, E_0. Let us now assume that this equilibrium solution is subjected to a small perturbation of the electron density, N', and of the electric field, E'. The evolution of the perturbations will be described by

$$\frac{\partial N'}{\partial t} + v_0 \frac{\partial N'}{\partial x} + N_0 \frac{\partial v'}{\partial x} = 0, \tag{57}$$

where $v_0 = -bE_0$. By a Fourier decomposition of the perturbation, Eq. (57) can be written as

$$(-\omega + v_0 k)\hat{N}'_k + kN_0\hat{v}'_k = 0, \tag{58}$$

where $\hat{N}'_k$ and $\hat{v}'_k$ are the Fourier components of the perturbations associated with the mode with wavenumber k. In Eq. (58), a temporal dependence of the form $e^{-i\omega t}$ is assumed for the Fourier components.

The Fourier components of the velocity and electric field perturbations are related as

$$\hat{v}'_k = -b\hat{E}'_k = bq_e\hat{N}'_k\hat{F}_k,$$

where q_e is the absolute value of the electron charge. Taking into account that F is a real odd function of its argument, the Fourier component $\hat{F}_k$is purely imaginary, $\hat{F}_k = i\Im(\hat{F}_k)$. Moreover, since $|F(x-x')|$ is a decreasing function of $|x-x'|$ and $F(x-x') > 0$ for $x - x' > 0$, it will be $\Im(\hat{F}_k) < 0$ for $k > 0$ and $\Im(\hat{F}_k) > 0$ for $k < 0$. Therefore, Eq. (58) can be rewritten as

$$\omega = v_0 k + ibq_e N_0 \Im(\hat{F}_k)k \tag{59}$$

and all modes will be damped down in the continuous system, since $\Im(\omega) < 0$.

When the effect of the discrete grid spacing, H, is taken into account [3], the filtered and aliased version of $\hat{v}'_k$ must be introduced in (58), resulting in the momentum-conserving scheme

$$(-\omega + v_0 k)\hat{N}'_k + kbq_e N_0 \hat{W}_k \hat{F}^{\mathrm{m}}_k \sum_{j=-\infty}^{j=\infty} \hat{N}'_{k+jk_g}\hat{W}_{k+jk_g} = 0, \tag{60}$$

where $k_g = 2\pi/H$, $\hat{W}_k$ is the Fourier component of the assignment function shape, and $\hat{F}^{\mathrm{m}}$ is the discretely sampled version of $\hat{F}$. Using the periodicity of $\hat{F}^{\mathrm{m}}_k$ [14], the dispersion relation may be written as

$$1 - ibq_e N_0 \Im\left(\hat{F}^{\mathrm{m}}_k\right) \sum_{j=-\infty}^{j=\infty} \frac{k_j \hat{W}^2_{k_j}}{\omega - v_0 k_j} = 0, \tag{61}$$

where $k_j = k + jk_g$. We always assume that the resolution is fine enough to achieve a good sampling of $\hat{F}^{\mathrm{m}}_k$ so that the properties of $\hat{F}(k)$ are equally valid for its discretely sampled version. In other words, $\hat{F}_k$ is band-limited to the principal zone $-\frac{1}{2}k_g < k < \frac{1}{2}k_g$.

In contrast, the dispersion relation for the energy-conserving interpolation scheme is found to be [14]

$$1 - i\frac{bq_e N_0 \Im\left(\hat{F}^{\mathrm{e}}_k\right)}{\sin\left(\frac{1}{2}kH\right)/\frac{1}{2}H} \sum_{j=-\infty}^{j=\infty} \frac{k_j^2 \hat{W}^2_{k_j}}{\omega - v_0 k_j} = 0, \tag{62}$$

where $\hat{F}^{\mathrm{e}}$ is the discretely sampled version of $\hat{F}$ that now relates charge density at the nodes of the grid to electric field at the cell boundaries.

A direct comparison between the dispersion relations of the energy-conserving and momentum-conserving schemes reveals a clear difference in the behavior of the aliases. Let us consider a simplified case where only a single alias is retained. Equations (61) and (62) can then be written, respectively, as

$$\omega = v_0 k_j + ibq_e N_0 \Im\left(\hat{F}^{\mathrm{m}}_k\right) k_j \hat{W}^2_{k_j}, \tag{63}$$

$$\omega = v_0 k_j + ibq_e N_0 \frac{\Im\left(\hat{F}^{\mathrm{e}}_k\right)}{\sin\left(\frac{1}{2}kH\right)/\frac{1}{2}H} k_j^2 \hat{W}^2_{k_j}. \tag{64}$$

The dispersion relation for the momentum-conserving scheme is linear in k_j. Therefore, the aliases with $j > 1$ and $j < -1$ will have $\Im(\omega) > 0$, provided that $-\frac{1}{2}k_g < k < 0$ and

$0 < k < \frac{1}{2}k_g$, respectively. This result shows that the modes k near the limit of the principal zone are likely to destabilize the momentum-conserving scheme, since the filtering of these modes inside the principal zone and the filtering of the first positive or negative alias are comparable [14]. In contrast, for the energy-conserving scheme, $\Im(\omega) < 0$ for all the aliases, since ω is quadratic in k_j and $\Im(\hat{F}_k^e)/\sin(\frac{1}{2}kH) < 0$, and all modes are damped down.

The zeros of the dispersion relations (62) and (61) have been obtained numerically by applying a Delves–Lyness algorithm [10, 19]. As expected, the inclusion of an alias beyond $k + k_g$ and $k - k_g$ gives rise to very small differences in $\Im(\omega)$. For each value k, three values of ω were found. In Fig. 9, the most unstable of these three solutions is shown for

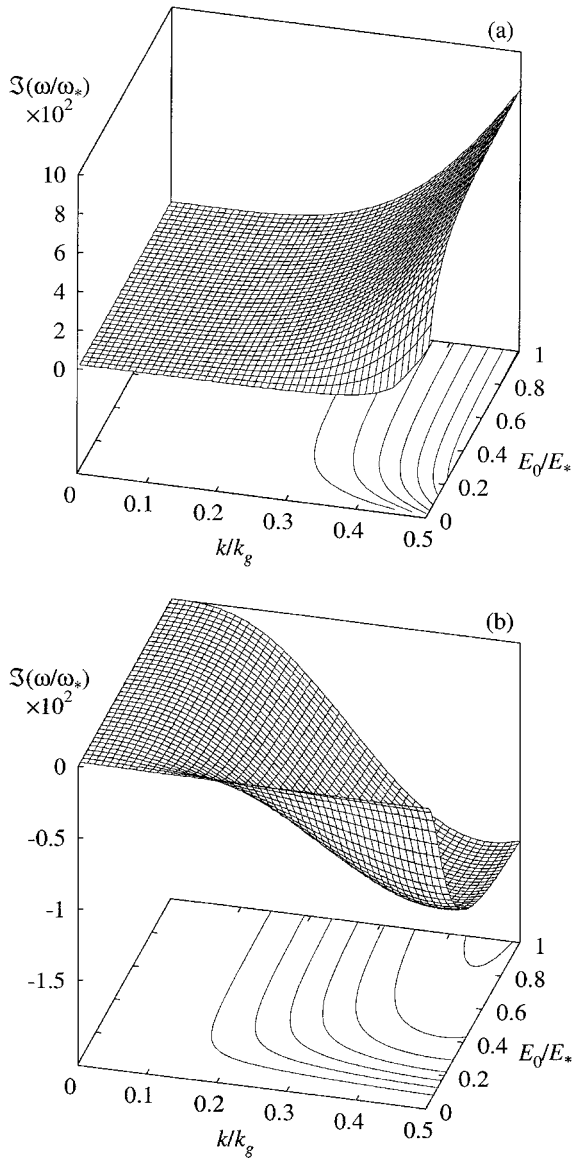

FIG. 9. Dimensionless growth rate of the perturbations corresponding to the most unstable mode for (a) momentum-conserving and (b) energy-conserving schemes of interpolation. The growth rate scale is defined as $\omega^* = k_g v^*$, where $v^* = bE^*$ and $E^* = q_e|\Im(\hat{F}_k)|N_0$.

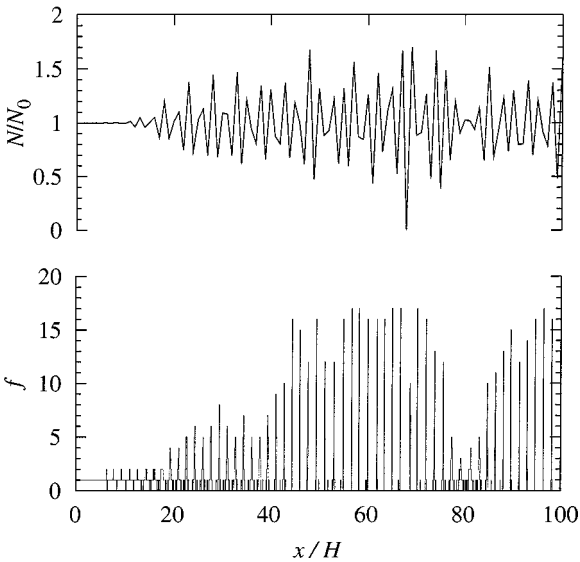

FIG. 10. Electron density distribution (upper graph) and number of computational particles per $1/10$ of cell (lower graph) at $t = 20t_0$, as predicted by the momentum-conserving PIC simulation.

both schemes. Clearly, the momentum-conserving scheme is unstable, particularly for large values of k, due to interaction with the first unstable $k \pm k_g$ aliases.

These results are in fair agreement with the instability arising in the momentum-conserving PIC simulation of Eq. (56). In the PIC simulation, the cylindrical discharge channel connects two infinite parallel plates separated by a distance L, which is divided in 100 computational cells. Electrons are continuously being injected at the cathode to maintain the constant initial electron density. The upper part of Fig. 10 shows the electron density distribution at $t = 20t_0$, with $t_0 = L/bE_0$. The instability observed in the particle density gives rise to the clustering of electrons in packets separated by a distance of $1.9H$ approximately. This spacing is smaller, but very close to $2H$, which is the minimum wavelength that can be sampled by the grid. This finding is consistent with our interpretation that the instability of the momentum-conserving PIC simulation is triggered by the first aliases $k \pm k_g$. The clustering can be observed in the lower part of Fig. 10, where the histogram of particle position is shown with a resolution of $H/10$.

ACKNOWLEDGMENTS

The authors acknowledge fruitful discussions with Dr. R. Morrow and Dr. F. Mesa during the development of this work.

REFERENCES

1. I. Abbas and P. Bayle, A critical analysis of ionizing wave propagation mechanisms in breakdown, *J. Phys. D. Appl. Phys.* **13**, 1055 (1980).
2. J. P. Boris and D. L. Book, Flux-corrected transport. III. Minimal-error FCT algorithms, *J. Comput. Phys.* **20**, 397 (1976).
3. J. U. Brackbill, The ringing instability in particle-in-cell calculations of low-speed flow, *J. Comput. Phys.* **75**, 469 (1988).

4. J. U. Brackbill and H. M. Ruppel, FLIP: A method for adaptatively zoned, particle-in-cell calculations of fluid flows in two dimensions, *J. Comput. Phys.* **65**, 314 (1986).
5. C. K. Bridsall and A. B. Langdon, *Plasma Physics via Computer Simulation* (IoP Publishing, Bristol, 1991).
6. D. Burgess, D. Sulsky, and J. U. Brackbill, Mass matrix formulation of the flip particle-in-cell method, *J. Comput. Phys.* **103**, 1 (1992).
7. A. Castellanos, A. T. Pérez, and P. Atten, Charge difussion versus Coulomb repulsion in finite amplitude electroconvection, in *1993 IEEE Industry Applications Society Annual Meeting*, IEEE Cat. No. 94CH2792-0 (1989), pp. 2112–2117.
8. R. Chicón, A. Castellanos, and E. Marín, Numerical modelling of coulomb-driven convection in insulating liquids, *J. Fluid Mech.* **344**, 43 (1997).
9. A. J. Davies, C. S. Davies, and C. J. Evans, Computer simulation of rapidly developing gaseous discharges, *Proc. Inst. Electr. Eng.* **118**, 816 (1971).
10. L. M. Delves and J. N. Lyness, A numerical method for locating the zeros of an analytic function, *Math. Comput.* **21**(100), 543 (1967).
11. S. K. Dhali and P. F. Williams, Two-dimensional studies of streamers in gases, *J. Appl. Phys.* **62**(12), 4696 (1987).
12. G. E. Georghiou, R. Morrow, and A. C. Metaxas, An improved finite-element flux-corrected transport algorithm, *J. Comput. Phys.* **148**, 605 (1999).
13. G. E. Georghiou, R. Morrow, and A. C. Metaxas, Two-dimensional simulation of streamers using the FE-FCT algorithm, *J. Phys. D. Appl. Phys.* **33**(3), L27 (2000).
14. R. W. Hockney and J. W. Eastwood, *Computer Simulaton Using Particles*. (Hilger, Bristol, 1988).
15. E. E. Kunhardt and C. Wu, Towards a more accurate flux corrected transport algorithm, *J. Comput. Phys.* **68**, 127 (1987).
16. A. B. Langdon, Effects of the spatial grid in simulation plasmas, *J. Comput. Phys.* **6,** 247 (1970).
17. G. Lapenta, F. Iinoya, and J. U. Brackbill, Particle-in-cell simulation of glow discharges in complex geometries, *IEEE Trans. Plasma Sci.* **23**(4), 769 (1995).
18. E. L. Lindman, Dispersion relation for computer simulated plasmas, *J. Comput. Phys.* **5**, 13 (1970).
19. R. Marqués, F. Mesa, and M. Horno, Non reciprocal and reciprocal complex and backward waves in parallel waveguides loaded with a ferrite slab arbitrarily magnetized, *IEEE Trans. Microwave Theory Tech.* **MTT-41**, 1409 (1993).
20. R. Morrow, Numerical solution of hyperbolic equations for electron drift in strongly non-uniform electric fields, *J. Comput. Phys.* **43**, 1 (1981).
21. R. Morrow, Theory of negative corona in oxygen, *J. Comput. Phys.* **32**, 1799 (1985).
22. R. Morrow and L. E. Cram, *Computational Techniques and Applications* (North-Holland, Amsterdam, 1984), pp. 719–729.
23. R. Morrow and L. E. Cram, Flux-corrected transport and diffusion on an non-uniform mesh, *J. Comput. Phys.* **57**, 129 (1985).
24. P. J. O'Rourke and J. U. Brackbill, On particle-grid interpolation and calculating chemistry in particle-in-cell methods, *J. Comput. Phys.* **109**, 37 (1993).
25. K. Yoshida and H. Tagashira, Computer simulation of a nitrogen discharge at high overvoltages, *J. Phys. D. Appl.-Phys.* **9**(3), 491 (1976).
26. M. Yousfi, A. Poinsignon, and A. Hamani, Finite element method for conservation equations in electrical gas discharge areas, *J. Comput. Phys.* **113**, 268 (1994).
27. S. T. Zalesak, Fully multidimensional flux-corrected transport algorithms for fluids, *J. Comput. Phys.* **31**, 335 (1979).